

A reduced moment-based model for oxygen precipitation in silicon

Bart C. Trzynadlowski and Scott T. Dunham
 University of Washington, Seattle, Washington 98195, USA

(Received 29 September 2013; accepted 2 December 2013; published online 26 December 2013)

A model for the precipitation of oxygen and associated dislocation loops in Czochralski-grown silicon is presented. Beginning with kinetic rate equations describing the growth and dissolution of oxide precipitates, a reduced model based on the moments of the precipitate size distribution is developed and validated against experimental data. The complete model source code is provided. Comparisons with the full, rate equation-based model show that the reduced version is comparably accurate, while requiring significantly less computational power. The formation of dislocation loops due to silicon interstitial ejection during precipitate growth is modeled using a simple, moment-based approach. An analysis of the sensitivity of the oxygen model to parameters is included. © 2013 AIP Publishing LLC. [<http://dx.doi.org/10.1063/1.4849435>]

I. INTRODUCTION

Oxygen is an important impurity that occurs in Czochralski-grown silicon.¹ Its effect on device yield and performance can be either beneficial or harmful. Oxygen is known to enhance the mechanical strength of silicon substrates and, in precipitated form, serves as a getter for metal contaminants, which can sharply degrade yield if located near the active regions of devices. Oxygen precipitation also leads to the formation of dislocation loops,^{2–4} which act as gettering sites but can also cause slip and warpage.⁵ Descriptions of precipitation behavior under a wide range of processing conditions exist in the literature.^{6–14} In recent years, there has been strong interest among solar cell manufacturers in understanding and controlling the impact of oxygen on carrier lifetime. Experiments show that oxide precipitates and complexes of boron and O₂ introduce strong recombination centers that substantially degrade cell efficiency.^{15–18}

Computational modeling has long been used by wafer suppliers and process engineers to optimize oxygen precipitation. Numerous models have been proposed but the most accurate are based on kinetic rate equations (KREs) and the physics of phase transformations. This approach requires solving dozens to hundreds of coupled differential equations, which is too slow to be practical in detailed process simulations involving 2D and 3D geometries. The Fokker-Planck equation is commonly used in practice but this method often requires writing custom solvers^{19–21} or devising boundary conditions with empirical fitting parameters.^{22,23} In our experience, published models are difficult to replicate and source code is rarely made available. It is known that oxygen precipitation is extremely sensitive to initial conditions²² but analyses of model sensitivity and stability are not usually reported.

We have developed a reduced model that tracks higher-order information about the precipitate size distribution (moments). This model retains many of the attractive properties of KRE-based approaches—namely, that it can account for the effects of thermal history and that most of its parameters have a physical interpretation—while requiring far fewer equations. Our source code is freely available and

implemented in MATLAB.²⁴ In this paper, we derive the reduced model, compare it against experimental data, conduct a basic sensitivity analysis, and discuss shortcomings and topics for future investigation.

II. MODEL

A. Full kinetic precipitation model

Oxygen precipitation can be modeled by tracking the concentrations of solute and each possible precipitate size with separate state variables. Nucleation—the initial formation of a precipitate from solute atoms—can occur either heterogeneously, requiring some existing defect or attachment site, or homogeneously, requiring only a supersaturation of the solute. Here, only homogeneous nucleation is considered. Two solute atoms cluster together to form a size two precipitate and then continue to either grow or dissolve one atom at a time. This is termed a *full kinetic precipitation model*.

The state variables are evolved over time and space by solving a system of KREs.

$$\frac{\partial C_O}{\partial t} = D_O \nabla^2 C_O - 2 \frac{\partial f_2}{\partial t} - \sum_{n=3}^{\infty} n \frac{\partial f_n}{\partial t}, \quad (1)$$

$$\frac{\partial f_n}{\partial t} = R_n - R_{n+1} \quad n = 2, 3, 4, \dots, \quad (2)$$

where C_O is the concentration of interstitial oxygen, our solute, and is described by a diffusion-reaction equation with diffusivity D_O because it is a mobile species. The concentration of precipitates containing n oxygen atoms is denoted by f_n . Precipitates are immobile and assumed to be spaced sufficiently far apart that direct interactions between them can be ignored. The net rate of growth from size $n - 1$ to n , R_n , links adjacent sizes. It is the difference between the growth and dissolution rates.

$$R_2 = g_1 C_O - d_2 f_2, \quad (3)$$

$$R_n = g_{n-1} f_{n-1} - d_n f_n, \quad (4)$$

where g_n is the rate of growth from size n to $n+1$ and d_n is the rate of dissolution from size n to $n-1$. Precipitates are modeled as spheres with radius r_n given by

$$r_n = \left(3n \frac{V_{SiO_2}}{4\pi} \right)^{1/3}, \quad (5)$$

where V_{SiO_2} is the molecular volume of SiO_2 . In reality, precipitates are more accurately described as oblate spheroids with variable aspect ratio.^{25–28} Suggestions for how this could be incorporated into a future version of the model are given in Sec. III.

A derivation of the growth and dissolution rates appears in Ref. 29. The expressions for diffusion-limited reactions are

$$g_n = \frac{4\pi \cdot r_n^2}{a + r_n} D_{OCo}, \quad (6)$$

$$d_n = g_{n-1} \exp\left(\frac{\Delta G_n - \Delta G_{n-1}}{k_B T}\right), \quad (7)$$

where a is on the order of the silicon lattice constant, k_B is Boltzmann's constant, and T is temperature. The total change in free energy upon forming a size n precipitate is ΔG_n and is discussed further below.

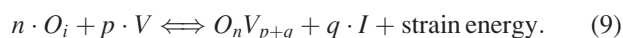
When implementing Eqs. (1) and (2) in simulation, a maximum precipitate size must be chosen. It must be large enough to ensure that its concentration remains negligible throughout the simulation. In our simulations, we used 10^9 atoms. Because it is not practical to solve more than a few hundred equations, the size space must be sampled and the equations discretized appropriately. There is a very high concentration gradient across the smallest sizes and to compute this accurately, unit sample spacing is used up to a size u . Beyond u , the spacing continually increases between adjacent samples. The size n_i of the i th sample is given by

$$n_i = \begin{cases} i & i \leq u \\ u + \sum_{j=u}^{i-1} S^{j-u} & i > u. \end{cases} \quad (8)$$

We used a value of 10 for u . S is the sample discretization factor. A value of 1 results in unit spacing and larger values create coarser spacing. Reasonable choices of S for a full kinetic precipitation model lie between 1.0 and 1.5. To account for non-unit sample spacing, Eqs. (1) and (2) are discretized according to the method described by Kobayashi in Appendix B of Ref. 30.

B. Strain and the role of point defects

Deriving the precipitate energy, ΔG_n , requires a more detailed discussion of the mechanics of oxygen precipitation. The formation of an oxide precipitate can be expressed by the following reaction:^{30,31}



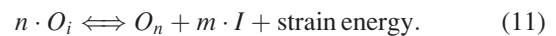
O_i is an interstitial oxygen atom, V is a silicon vacancy, and I is a silicon interstitial. The quantities p and q are the numbers of these defects involved in the reaction, and $O_n V_{p+q}$ refers to an oxide precipitate containing n oxygen atoms that has consumed p vacancies and ejected q interstitials.

As their name implies, oxide precipitates are comprised of SiO_2 (although they are sometimes less accurately referred to as *oxygen* precipitates). The molecular volume of SiO_2 exceeds the atomic volume of crystalline silicon, meaning that either additional volume must be supplied to accommodate the expanding precipitate, or the matrix and precipitate become compressed, storing energy in a strain field. Point defects can provide volume: vacancies can be absorbed or interstitials can be ejected at a free energy cost. The optimal (i.e., minimum energy cost) solution is a balance between interacting with point defects and retaining some residual strain energy.

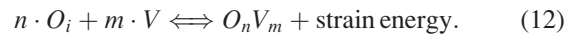
We assume fast interstitial/vacancy recombination so that

$$C_I C_V \cong C_I^* C_V^*. \quad (10)$$

The silicon interstitial and vacancy concentrations are C_I and C_V , respectively; C_I^* and C_V^* are their thermal equilibrium values. This allows us to use a simplified reaction, as others have,^{19,21,32} involving only interstitials:



This is equivalent to considering



Our model tracks only the *net* interstitial concentration, N_I .

$$N_I = C_I - C_V. \quad (13)$$

Using Eqs. (10) and (13), C_I and C_V can be expressed as functions of N_I , C_I^* , and C_V^* .

C. Energetics of oxide precipitates

To derive the precipitate formation energy, we begin with the vacancy-based form of the reaction, Eq. (12). In equilibrium, the energies of both sides of the reaction must balance:

$$\begin{aligned} n \cdot \Delta G_{O_i}^f + n k_B T \ln\left(\frac{C_{O_i}}{C_{Si}^*}\right) + m \cdot \Delta G_V^f + m k_B T \ln\left(\frac{C_V}{C_{Si}^*}\right) \\ = \Delta G_{n,m}^f + k_B T \ln\left(\frac{f_{n,m}^*}{C_{Si}^*}\right). \end{aligned} \quad (14)$$

Here, $\Delta G_{O_i}^f$ is the formation energy of interstitial oxygen. We define all formation energies relative to perfect silicon with oxygen in interstitial form, so this quantity is zero by definition. The vacancy formation energy is ΔG_V^f , $\Delta G_{n,m}^f$ is the formation energy of an oxide precipitate, and C_{Si} is the density of silicon lattice sites. The concentration of

precipitates having n oxygen atoms and incorporating m vacancies is $f_{n,m}$, and $f_{n,m}^*$ is the thermal equilibrium concentration. This is more general and technically more accurate than considering only f_n but we will later show that tracking all possible vacancy configurations is unnecessary. Rearranging and simplifying the equation leads to

$$-k_B T \ln \left(\frac{f_{n,m}^*}{C_{Si}} \right) = -nk_B T \ln \left(\frac{C_O}{C_{Si}} \right) - mk_B T \ln \left(\frac{C_V}{C_V^*} \right) + \Delta G_{n,m}^f. \quad (15)$$

The right-hand side of Eq. (15) is $\Delta G_{n,m}$, the total free energy change upon formation of a precipitate. The precipitate formation energy can be broken down further^{19,21}

$$\Delta G_{n,m}^f = n \cdot \Delta G_P + \Delta G_{n,m}^{strain} + \Delta G_n^{surface}, \quad (16)$$

$$\Delta G_n^{surface} = 4\pi \cdot r_n^2 \alpha, \quad (17)$$

$$\Delta G_{n,m}^{strain} = 6 \frac{4}{3} \pi \cdot r_n^3 \mu_{Si} \frac{e_T^2(n, m)}{1 + 4\mu_{Si}/(3K_{SiO_2})}, \quad (18)$$

$$e_T(n, m) = \left[\frac{V_{SiO_2} \cdot n/2}{V_{Si} \cdot (n/2 + m)} \right]^{1/3} - 1, \quad (19)$$

where ΔG_P is the volume component of the precipitate formation energy and is obtained directly from the solubility,

$$C_{SS} = C_{Si} \exp \left(\frac{\Delta G_P}{k_B T} \right). \quad (20)$$

The surface energy parameter, α , is usually reported in units of J/m². The transformation strain (or linear misfit strain), e_T , quantifies the mismatch relative to perfect silicon of a size (n, m) precipitate. The shear modulus of silicon is μ_{Si} , K_{SiO_2} is the bulk modulus of SiO₂, and V_{Si} is the atomic volume of silicon.

Although a precipitate can theoretically be formed by absorbing any number of vacancies, the energetics are unfavorable for all but a narrow range near the optimal size, m_{opt} .³⁰ This size can be found by minimizing the energy, $\Delta G_{n,m}$, with respect to m : differentiate, set equal to zero, and solve for m_{opt} . Unfortunately, the result is an equation without a closed-form solution.

To simplify this equation, we assume that the precipitate is nearly relaxed, with only a small residual strain. Therefore, m_{opt} should be close to m_0 , the number of vacancies needed to fully compensate for the excess precipitate volume (leaving zero residual strain). This zero strain point can be readily obtained by setting Eq. (19) to zero and solving for $m = m_0$. We then write a linear approximation for e_T using a Taylor series expanded about m_0

$$e_T(n, m) \cong e_T(n, m_0) + e'_T(n, m_0) \cdot (m - m_0), \quad (21)$$

where e'_T is the first derivative of e_T with respect to m . Using the linearized e_T , m_{opt} (a function of n) is found to be

$$m_{opt}(n) \cong \frac{n}{2} \left[\frac{3}{4} k_B T \ln \left(\frac{C_V}{C_V^*} \right) \cdot \left(\frac{V_{SiO_2}}{V_{Si}^2 \mu_{Si}} \right) \times \left(1 + \frac{4\mu_{Si}}{3K_{SiO_2}} \right) + \frac{V_{SiO_2}}{V_{Si}} - 1 \right]. \quad (22)$$

Figure 1 demonstrates the validity of this approach by showing the error of Eq. (22), along with that of precipitate energies calculated using this approximation, relative to the true value of m_{opt} . The error increases with increasing point defect supersaturation and temperature but the curves are virtually independent of n . The temperature used to generate the plot (1050 °C) corresponds to a typical growth temperature used in two-step precipitation tests. The plot reveals that the dependence of the precipitate energy on m is relatively weak and that even large errors in m_{opt} have a modest effect on precipitate energy.

For all but the smallest precipitate clusters, we assume that only m_{opt} vacancies are incorporated because any other value will raise the formation energy and therefore be less likely. This allows us to write

$$f_n = \sum_m f_{n,m} \cong f_{n,m_{opt}} \quad (23)$$

which at last leads to the definition of ΔG_n

$$\Delta G_n = -nk_B T \ln \left(\frac{C_O}{C_{Si}} \right) + m_{opt} k_B T \ln \left(\frac{C_I}{C_I^*} \right) + \Delta G_n^f, \quad (24)$$

where ΔG_n^f is $\Delta G_{n,m}^f$ evaluated at $m = m_{opt}$ and Eq. (10) has been used to rewrite the point defect energy in terms of interstitials.

D. Small clusters

At the smallest sizes, the properties of oxygen clusters are expected to deviate from the larger, *macroscopic* precipitates described up to this point. They may form different structures, such as thermal double donors^{33,34} or highly

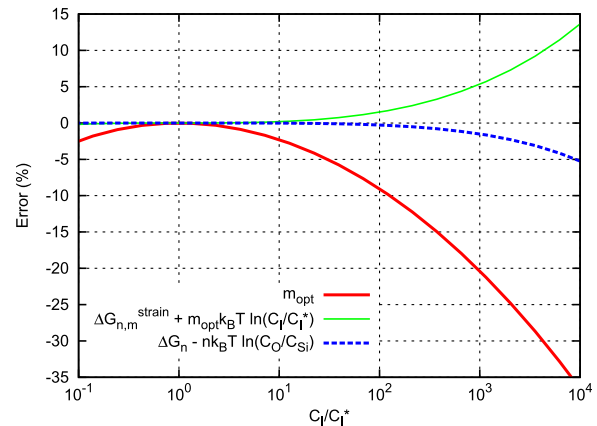


FIG. 1. The error between the true value of m_{opt} and the approximation of Eq. (22) along with the effect on precipitate energy at $T = 1050^\circ\text{C}$ with $n = 10^6$. The dependence of the curves on n is negligible. According to simulations, the observed range of C_I/C_I^* in the experiments analyzed in this work is approximately between 1 and 10^3 .

mobile O₂ dimers,^{35–37} and evolve orthogonally to precipitates. They may also bind to other impurities, as in the case of BO₂ complexes, which act as strong recombination centers and have been implicated in the degradation of solar cells.^{18,38}

We model the discrete effects of small oxygen clusters by considering likely O_nV_m complexes and estimate their formation energies ($\Delta G_{n,m}^f$) using a simple heuristic and *ab initio* calculations of O₂, OV, O₂V, and VV (di-vacancy) clusters performed with VASP.³⁹ We assume that the *m*-states for a size *n* small cluster are in relative thermal equilibrium with each other, allowing us to obtain a single expression for total energy by using the following relationships:

$$f_n^* = C_{Si} \exp\left(\frac{-\Delta G_n}{k_B T}\right) = \sum_{m=0}^n f_{n,m}^*, \quad (25)$$

$$f_{n,m}^* = C_{Si} \exp\left(\frac{-\Delta G_{n,m}}{k_B T}\right). \quad (26)$$

In our model, only sizes two and three are implemented this way. To enforce continuity from size three to size four, where macroscopic energies are used, an offset is applied to the macroscopic energies making them equal to the small cluster energy at size three. For further detail, we refer the reader to our MATLAB code.²⁴

E. Reduced kinetic precipitation model

Full kinetic precipitation models are impractical for large-scale process simulations because of the large number of equations that must be solved at each spatial grid point. A *reduced kinetic precipitation model* preserves many of the advantages of a full model, such as the ability to account for the effects of thermal history, but tracks only the moments of the distribution.⁴⁰ The *i*th moment is defined as

$$m_i = \sum_{n=k}^{\infty} n^i f_n. \quad (27)$$

Precipitates below size *k* are solved as in the full model. The zeroth moment, *m*₀, is the concentration of all precipitates of size *k* or larger. The first moment, *m*₁, is the concentration of all oxygen atoms held in those precipitates. The second moment, *m*₂, contains information about the breadth of the distribution. In this work, only the lowest two moments are used and *k* was chosen to be 72. Following the approach in Ref. 40, we can write

$$\frac{\partial C_O}{\partial t} = D_O \nabla^2 C_O - \frac{\partial m_1}{\partial t} - 2 \frac{\partial f_2}{\partial t} - \sum_{n=3}^{k-1} n \frac{\partial f_n}{\partial t}, \quad (28)$$

$$\frac{\partial m_0}{\partial t} = R_k, \quad (29)$$

$$\frac{\partial m_1}{\partial t} = k \cdot R_k + d_k f_k + D_O m_0 \cdot (C_O \gamma_2 - \gamma_3), \quad (30)$$

$$\gamma_2 = \frac{1}{D_O C_O m_0} \sum_{n=k}^{\infty} g_n f_n, \quad (31)$$

$$\gamma_3 = \frac{1}{D_O m_0} \sum_{n=k}^{\infty} d_n f_n. \quad (32)$$

The second term in the right-hand side of Eq. (30) is required to correct for duplication between *R_k* and γ_3 . In order to avoid explicitly solving for sizes *k* and above, γ_2 and γ_3 must somehow be expressed only in terms of the moments and state variables excluding *f_{k+1}* and higher. The *delta function approximation* (DFA), wherein the size distribution above size *k* is assumed to be sharply peaked about the average size and is approximated by a Dirac delta function, satisfies this requirement.⁴¹ By assuming that

$$f_n = m_0 \cdot \delta(n - n_{avg}), \quad (33)$$

$$n_{avg} = \frac{m_1}{m_0}, \quad (34)$$

γ_2 and γ_3 are reduced to

$$\gamma_2 = \frac{g_{n_{avg}}}{D_O C_O}, \quad (35)$$

$$\gamma_3 = \frac{d_{n_{avg}}}{D_O}. \quad (36)$$

Because *f_k* appears in the reduced model but can no longer be solved directly (it is included within the moments), an estimator must be devised. Using the full model, we generated data for a wide range of representative experimental conditions and extracted the moments. After investigating many different predictors based on *m*₀, *m*₁, *f_{k-1}*, *f_{k-2}*, and *C_I/C_I**, we found that the following empirical function works reasonably well:

$$f_k = \frac{m_0}{([p_0 \cdot (n_{avg} - k)]^p) \cdot (n_{avg} - k) + 1}, \quad (37)$$

where *p* and *p*₀ are fitting parameters. This function behaves correctly in the limiting cases

$$\lim_{n_{avg} \rightarrow k} f_k = m_0, \quad \lim_{n_{avg} \rightarrow \infty} f_k = 0. \quad (38)$$

F. Dislocation loops

Faulted dislocation loops are known to form in the vicinity of oxide precipitates due to high interstitial supersaturations caused by interstitial ejection and precipitate stress fields. Each macroscopic precipitate will eject *m_{opt}(n)* interstitials. To simplify our implementation, we eject *n/2* interstitials for each precipitate (we have observed that *m_{opt}/n* ranges between approximately 0.4 and 0.6), although we continue to use *m_{opt}* when computing energy. This allows us to write the equation for *N_I* as

$$\begin{aligned} \frac{\partial N_I}{\partial t} = & D_I \nabla^2 C_I - D_V \nabla^2 C_V - R_I^{surface} \\ & - \frac{\partial m_1^{DL}}{\partial t} + 0.5 \frac{\partial m_1}{\partial t} + \sum_{n=4}^{k-1} 0.5n \frac{\partial f_n}{\partial t}, \end{aligned} \quad (39)$$

where D_I and D_V are the interstitial and vacancy diffusivities, respectively, and $R_I^{surface}$ is the surface boundary condition.

High interstitial concentrations impede precipitation by increasing precipitate energy. Once dislocations are formed, interstitials are absorbed into the stacking faults, lowering C_I/C_I^* and allowing precipitation to proceed. We implement a simple dislocation model, described by the subsequent two equations, which nucleates only at the critical size and assume that once nucleated, dislocations are stable and will not dissolve. They may grow or shrink in size, however.

$$\frac{\partial m_0^{DL}}{\partial t} = g_{DL}(n_C^{DL}) \cdot f_{DL}^*(n_C^{DL}), \quad (40)$$

$$\frac{\partial m_1^{DL}}{\partial t} = n_C^{DL} \cdot \frac{\partial m_0^{DL}}{\partial t} + g_{DL}(n_{avg}^{DL}) \cdot m_0^{DL} - d_{DL}(n_{avg}^{DL}) \cdot m_1^{DL}. \quad (41)$$

The moments (m_0^{DL} and m_1^{DL}) are analogous to their oxygen counterparts. The critical size, n_C^{DL} , is the size above which dislocation loops will grow and below which they will shrink. It is the value of n that satisfies

$$\frac{\partial \Delta G_n^{DL}}{\partial n} = 0, \quad (42)$$

where ΔG_n^{DL} , the total free energy of a size n dislocation loop, is

$$\Delta G_n^{DL} = -nk_B T \ln\left(\frac{C_I}{C_I^*}\right) + n \cdot \Delta G_{SF} + n \cdot \Delta G_{DL}^{strain}(n_{avg}) + \Delta G_n^{self}, \quad (43)$$

$$\Delta G_n^{self} = \frac{r_n^{DL}}{\sqrt{2}} \frac{\pi K_{DL}}{2b^2} \left[\ln\left(8 \frac{r_n^{DL}}{r_{core}}\right) - 1 \right], \quad (44)$$

$$\Delta G_{DL}^{strain}(n) = -V_{Si} \Delta \epsilon_{SF} \sigma_n. \quad (45)$$

Here, ΔG_{SF} is the per-atom formation energy of a stacking fault, obtained using VASP, and ΔG_n^{self} is the dislocation elastic self-energy. The energy coefficient, K_{DL} , accounts for the anisotropy of silicon, b is the magnitude of the Burgers vector, and r_{core} is the dislocation core radius, which we set equal to b .⁴² The $1/\sqrt{2}$ factor appears in Eq. (44) because we assume that dislocations nucleated at the surface of an oxide precipitate will take on a semi-circular geometry. The dislocation radius as a function of the number of atoms n is

$$r_n^{DL} = a_{Si} \cdot \left(\frac{n\sqrt{3}}{8\pi}\right)^{1/2}, \quad (46)$$

where a_{Si} is the silicon lattice constant. Extrinsic stacking faults impart a considerable amount of compressive strain on the surrounding matrix and their formation energy is therefore highly dependent on local stress. Tensile stress, as generated at the surface of a precipitate, promotes stacking fault formation. The per-atom change in energy of a stacking fault formed at the surface of a size n oxide precipitate is $\Delta G_{DL}^{strain}(n)$. The stacking fault induced strain, $\Delta \epsilon_{SF}$, is the

strain caused by a fully relaxed stacking fault along the direction of its {111} habit plane normalized to atomic volume. It was extracted from a VASP calculation. The stress tangential to the surface of a precipitate is²⁰

$$\sigma_n = \frac{6\mu_{Si} K_{SiO2}}{3K_{SiO2} + 4\mu_{Si}} \cdot e_T(n, m_{opt}(n)). \quad (47)$$

A closed-form solution for n_C^{DL} does not exist. To compute it quickly, we begin with an initial guess (10^4) and iterate 6 times. This computation can be written in inline form and performed very efficiently.

The equilibrium concentration of dislocation loops at the critical size, $f_{DL}^*(n_C^{DL})$, determines the nucleation rate:

$$f_{DL}^*(n) = 4 \frac{2\pi \cdot r_n^{DL}}{a} \cdot (m_0 - m_0^{DL}) \cdot \exp\left(\frac{-\Delta G_n^{DL}}{k_B T}\right). \quad (48)$$

Nucleation occurs heterogeneously at the surface of oxide precipitates. A factor of 4 is present to account for each possible {111} orientation. The growth and dissolution rates are

$$g_{DL}(n) = D_I \lambda_n C_I, \quad (49)$$

$$d_{DL}(n) = g_{DL}(n-1) \cdot \exp\left(\frac{\partial \Delta G_n^{DL} / \partial n}{k_B T}\right), \quad (50)$$

where λ_n is a kinetic factor for the growth of a disk-shaped precipitate,⁴³

$$\lambda_n = \frac{4\pi^2 a_{Si} \cdot \left(\frac{n\sqrt{3}}{8\pi}\right)^{1/2}}{\ln\left(\frac{8a_{Si}}{a_{DL}} \left(\frac{n\sqrt{3}}{8\pi}\right)^{1/2}\right)}, \quad (51)$$

$$a_{DL} = \frac{\sqrt{3}}{4} a_{Si}, \quad (52)$$

where a_{DL} is the capture radius for interstitial attachment to the core, which we set to the silicon bond length.

III. RESULTS

A. Comparison of reduced and full models

The reduced model is expected to differ from the full model in two areas: formation of size k precipitates, which add to m_0 , and growth, which affects m_1 . Formation of size k precipitates is governed by R_k in Eq. (29). Growth of existing precipitates is governed by γ_2 and γ_3 , which in turn are obtained with the DFA. By comparing the behavior of the reduced and full models under identical conditions, it is possible to identify sources of mismatch.

Due to a lack of information on initial precipitate size distributions, we were not able to compare under conditions that replicate published experiments. A given set of initial m_0 and m_1 values, used to fit to experimental data, may correspond to many possible distributions in the full model. Therefore, we compare the models with no initial precipitation.

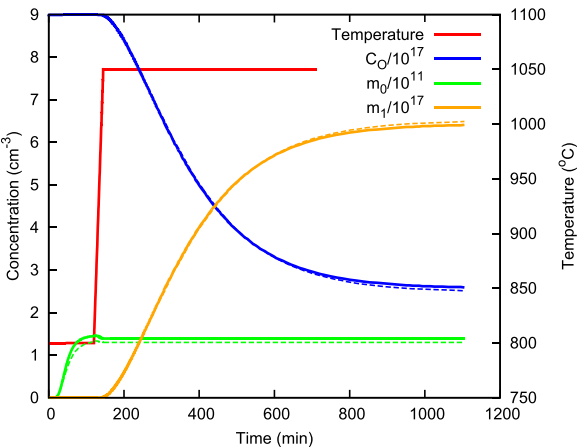


FIG. 2. Comparison between full (solid lines) and reduced (dashed lines) models for a two-step process: 800 °C for 2 h, 1050 °C for 16 h. Two regimes are visible: nucleation, where oxide precipitates (m_0) form, and growth, where the concentration of oxygen atoms contained in precipitates (m_1) increases as interstitial oxygen (C_O) is absorbed.

The validity of the DFA is easily tested by replacing the estimated f_k with the actual value computed simultaneously using the full model. We find the agreement to be very good—the solute concentration, m_0 , and m_1 all track their full model counterparts very accurately, indicating that the DFA is a sound approach for modeling the growth of large precipitates. We believe that mismatch between the models is caused primarily by the inaccuracy of R_k .

Figure 2 shows the evolution of the solute concentration, m_0 , and m_1 for both the reduced and full models during a two-step process. The agreement is similarly good for the

other experiments replicated in this work. The model parameters are listed in Table I.

All of our results are reported assuming a discretization factor S of approximately 1.11. This produces 196 equations in the full model (which serves as the base case for performance comparisons) and 35 in the reduced model. On a workstation equipped with a 3.2 GHz Intel Core i5-2500K processor running MATLAB 7.0.1 on Windows 7, the reduced model is faster by a factor of about 15. S can be increased to 1.21 (115 equations in the full model, 28 in the reduced model) without noticeably degrading accuracy, in which case the reduced model is faster by a factor of about 9.4. It is 23 times faster than the base case.

B. Comparison of reduced model to experiment

Final calibration of the model parameters (the surface energy, α , and the solubility, C_{SS}) was performed using the reduced model. The results appear in Table I. We allow α to have a linear temperature dependence and report it at two different temperatures: 750 °C (α_{750}) and 1050 °C (α_{1050}). Our fitted α increases with temperature as it does in Ref. 21 but opposite to Ref. 44.

We focused on experiments in the literature that measure changes in interstitial oxygen concentration using Fourier transform infrared spectroscopy because of its consistency and reliability. All data were interpreted using the new (i.e., 1983) ASTM calibration standard.⁴⁵ We looked primarily at two-step experiments, where thermal history was well described, there were no oxidizing anneals, and carbon and nitrogen calibration were negligible. All

TABLE I. Model parameter values.

Parameter	Value	Description	Reference
D_O	$0.13 \exp(-2.53 \text{ eV}/k_B T) \text{ cm}^2/\text{sec}$	Interstitial oxygen diffusivity	52
a	5.0 \AA	Interface reaction constant	
C_{SS}	$1.17 \times 10^{23} \exp(-1.499 \text{ eV}/k_B T) \text{ cm}^{-3}$	Oxygen solubility	
D_I	$51.4 \exp(-1.77 \text{ eV}/k_B T) \text{ cm}^2/\text{sec}$	Interstitial silicon diffusivity	53 and 54
C_I^*	$2.9 \times 10^{24} \exp(-3.18 \text{ eV}/k_B T) \text{ cm}^{-3}$	Interstitial silicon thermal equilibrium concentration	53 and 54
D_V	$3.07 \exp(-2.12 \text{ eV}/k_B T) \text{ cm}^2/\text{sec}$	Vacancy diffusivity	53 and 54
C_V^*	$1.4 \times 10^{24} \exp(-2.44 \text{ eV}/k_B T) \text{ cm}^{-3}$	Vacancy thermal equilibrium concentration	53 and 54
C_{Si}	$5.0 \times 10^{22} \text{ cm}^{-3}$	Silicon lattice site density	55
a_{Si}	5.431 \AA	Silicon lattice constant	55
V_{Si}	$2.0 \times 10^{-23} \text{ cm}^3$	Silicon atomic volume	55
μ_{Si}	64.9 GPa	Silicon shear modulus	56
V_{SiO2}	$4.35 \times 10^{-23} \text{ cm}^3$	SiO ₂ molecular volume	57
K_{SiO2}	36.9 GPa	SiO ₂ bulk modulus	58
b	$a_{Si} \sqrt{3}/3$	Magnitude of dislocation Burgers vector	
r_{core}	b	Dislocation core radius	
K_{DL}	72 GPa	Dislocation core energy coefficient	42 and 59
ΔG_{SF}	0.0152 eV	Stacking fault per-atom formation energy	
$\Delta \epsilon_{SF}$	0.996	Stacking fault induced strain	
p_0	5×10^{-3}	Fitting parameter for f_k estimator	
p	2	Fitting parameter for f_k estimator	
α_{750}	0.2394 J/m ²	Oxide precipitate surface energy at 750 °C	
α_{1050}	0.3206 J/m ²	Oxide precipitate surface energy at 1050 °C	
k	72	Size (atoms) at which RKPM model begins	
u	10	Size (atoms) beyond which size space is sampled	
S	1.106954	Sample discretization factor	

TABLE II. Fitted initial conditions used to replicate experimental data.

Source	Initial m_0 (cm^{-3})	Initial n_{avg}	Initial N_I (cm^{-3})
Chiou and Shive ⁶	1.00×10^{10}	7.80×10^3	-3.38×10^{12}
Swaroop <i>et al.</i> ⁸	1.0×10^8	9.53×10^3	-7.92×10^{11}
Kennel ⁴⁷	1.0×10^8	4.05×10^3	-4.45×10^{12}
Stewart ⁵⁰	1.0×10^8	4.05×10^3	-2.81×10^{14}

experiments were conducted on as-grown Czochralski silicon wafers. We assumed that initial conditions (m_0 , precipitate size, and net interstitial concentration) varied between different batches of samples and treated them as fitting parameters. Our simulations replicated thermal treatments as they were described, including temperature ramps. Table II lists the fitted initial conditions used for each experiment. In all of these simulations, we considered the wafer to be a 0D (single point) system, which eliminated diffusion terms in our equations.

Our model was calibrated against the two-step precipitation tests by Chiou and Shive,⁶ and Swaroop *et al.*⁸ These simple experiments are designed to simulate more complex processes, such as the CMOS process.⁴⁶ Their characteristic S-shape (precipitated oxygen on the y-axis, initial interstitial oxygen on the x-axis) allows the solubility to be readily extracted. The linear portion of the curve occurs in the regime of high oxygen supersaturation and can be extrapolated to the x-intercept to obtain the solubility at the growth temperature. Figures 3 and 4 show good agreement with two-step experiments. Precipitates are nucleated during the low temperature step and then grow and ripen during the long high temperature step.

Experiments conducted by Kennel⁴⁷ to investigate the effect of varying the durations of the nucleation and 1100 °C growth steps were also simulated. We find good agreement between our model and the data for 0 and 2 h nucleation steps at 750 °C, shown in Figure 5, but poorer agreement at 8 and 32 h. Simulation results for 650 °C nucleation treatments do not match Kennel's measurements. We believe these mismatches are due to the nucleation rate being too low, perhaps because we model precipitates as spheres when, in fact, they are needle- or platelet-shaped below 950 °C,^{26,27,48} or

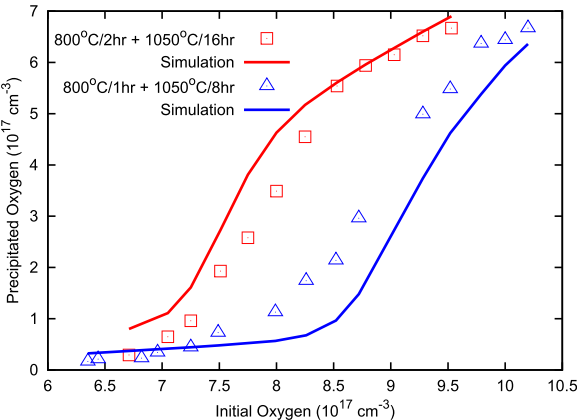


FIG. 3. Comparison of the reduced model to two-step precipitation tests by Chiou and Shive.⁶

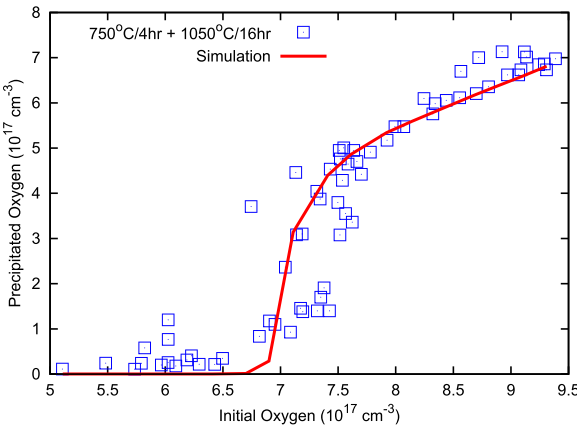


FIG. 4. Comparison of the reduced model to a two-step precipitation test by Swaroop *et al.*⁸

because the oxygen diffusivity at low temperatures is too low.

Experimental evidence for enhanced oxygen diffusivity at and below 650 °C exists but using the values reported in Ref. 49 did not substantially improve our fit. Alternative explanations for the discrepancies between theory and observations at low temperatures have also been advanced.¹³ Sueoka *et al.* found that assuming spherical geometry can cause nucleation rates to be underestimated.²² They model precipitates as oblate spheroids with an aspect ratio, β , that minimizes the sum of the strain and surface energies. The same approach could be used to extend our moment-based model. Modeling the surface energy, α , as a non-linear function of temperature may also allow some of the effects of morphology to be captured.

Simulation results of a one-step treatment at 750 °C are consistent with data from Stewart *et al.*⁵⁰ and are shown in Figure 6.

C. Sensitivity analysis

In order to assess the sensitivity of our model to changes in physical parameters (C_{SS} , α) and initial conditions (m_0 , n_{avg} , N_I), we performed a one-at-a-time sensitivity analysis.

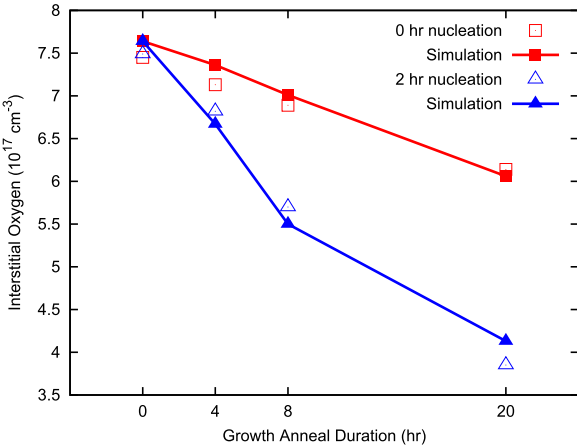


FIG. 5. Experimental and simulation results of the effect of varying the durations of 750 °C nucleation and 1100 °C growth anneals on the final interstitial oxygen concentration. Data from Ref. 47.

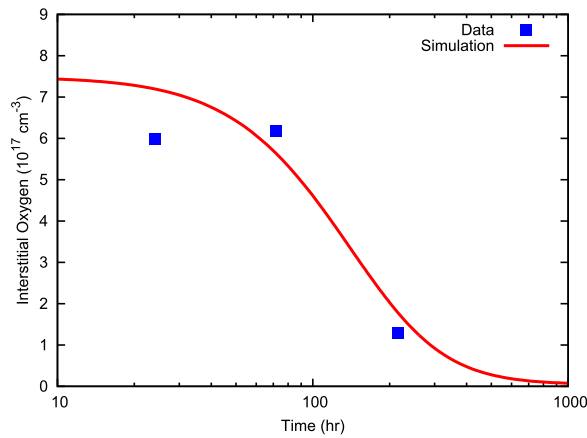


FIG. 6. Simulation results of the oxygen concentration over the course of a long-duration 750 °C anneal compared to SANS measurements.⁵⁰

Beginning with the best-fit parameters from a particular experiment, we varied each one, while keeping the others constant, and examined the effect on the fit. Our fitness metric, F , is a scaled sum-of-squares error,

$$F = \sum_i \left(\frac{y_i}{10^{18}} - \frac{x_i}{10^{18}} \right)^2, \quad (53)$$

where x_i is the experimental result at the i th sample point (precipitated oxygen concentration) and y_i is the corresponding simulation result. Because the valid range of each parameter can vary dramatically in magnitude, we introduce scaled parameters (A_{750} , A_{1050} , C_{750} , C_{1050} , M_0 , N , P) to normalize them:

$$\alpha_{750} = A_{750}/2, \quad \alpha_{1050} = A_{1050}/2, \quad (54)$$

$$C_{SS}(T = 750^\circ\text{C}) = 10^{15} \cdot 100^{C_{750}}, \quad (55)$$

$$C_{SS}(T = 1050^\circ\text{C}) = 10^{17} \cdot 10^{C_{1050}},$$

$$m_0 = 10^{8M_0}, \quad n_{avg} = k + 10^{4N}, \quad (56)$$

$$N_I = 10^{-3P} \cdot [C_I^*(T = 1200^\circ\text{C}) - C_V^*(T = 1200^\circ\text{C})]. \quad (57)$$

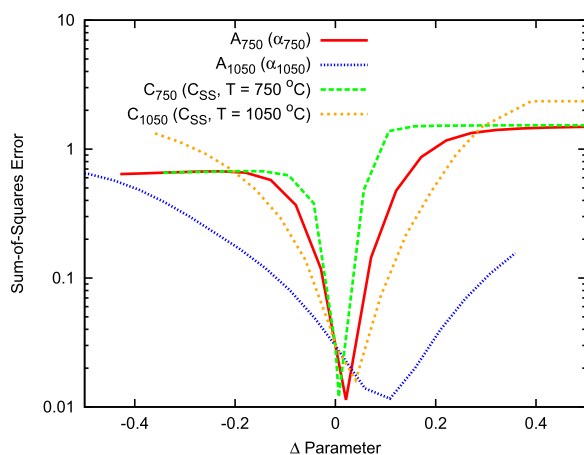


FIG. 7. One-at-a-time sensitivity analysis of the longer two-step test (750 °C/2 h + 1050 °C/16 h) by Chiou and Shive.⁶ The sum-of-squares error is plotted against the deviation from the scaled best-fit physical parameters.

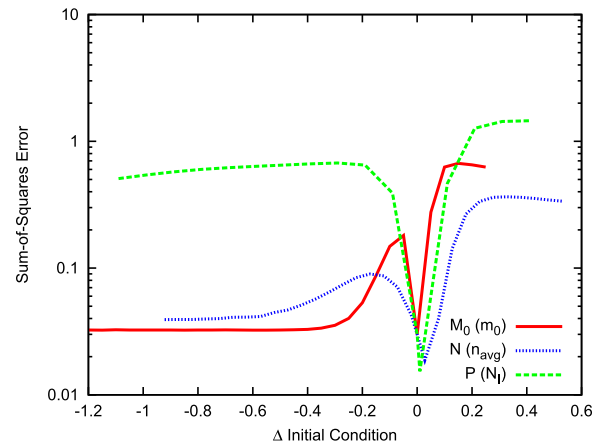


FIG. 8. One-at-a-time sensitivity analysis of the longer two-step test by Chiou and Shive⁶ measuring the impact of initial conditions.

These were also used by the optimizer to search for the best fit.

In Figure 7, the scaled physical parameters were varied within a realistic range for the longer of the two-step precipitation tests by Chiou and Shive.⁶ The deviation of the parameters is plotted and centered horizontally about zero, the best-fit value of each parameter. The procedure was repeated in Figure 8 with initial conditions. The model exhibits low to moderate sensitivity to most parameters during two-step precipitation tests. The surface energy and initial point defect concentrations have the strongest impact. Simulation results are insensitive to the initial precipitate concentration and average size over a wide range until either value becomes relatively large. This is consistent with experimental studies, where high concentrations of very large in-grown precipitates are not observed.⁵¹

Our best fits are not necessarily globally optimal. Changes in physical parameters or initial conditions can often be compensated by varying the remaining fitting parameters, although the results are not necessarily physically plausible nor are they consistent across all experiments. Because the surface energy was fit to experimental data, it absorbs some of the inaccuracies of our model.

IV. CONCLUSION

We have demonstrated a high performance reduced kinetic precipitation model for oxygen. Our model is able to successfully replicate experimental data using only the initial precipitate concentration, average size, and net interstitial concentration as fitting parameters. As with approaches based on discrete KREs and the Fokker-Planck equation, most of our model parameters have a physical interpretation. The reduced model requires far fewer equations, however, and consequently consumes significantly less run time. Our source code is freely available.²⁴ We believe that our moment-based approach has good potential for making precipitation models efficient enough to be used in large-scale TCAD simulations alongside other defect models. Using data on recombination sites associated with oxide precipitates and dislocation loops (such as the findings in Refs. 16 and 17) would make it possible to explore the variation in carrier

lifetime—and therefore, device performance—as a function of precipitation.

ACKNOWLEDGMENTS

Funding for this work was generously provided by SiWEDS, Sony Corp., and the Semiconductor Research Corp.

- ¹A. Borghesi, B. Pivac, A. Sassella, and A. Stella, "Oxygen precipitation in silicon," *J. Appl. Phys.* **77**(9), 4169–4244 (1995).
- ²W. Patrick, E. Hearn, W. Westdorp, and A. Bohg, "Oxygen precipitation in silicon," *J. Appl. Phys.* **50**(11), 7156 (1979).
- ³F. A. Ponce, T. Yamashita, and S. Hahn, "Structure of thermally induced microdefects in Czochralski silicon after high-temperature annealing," *Appl. Phys. Lett.* **43**(11), 1051 (1983).
- ⁴T. Ono, G. A. Rozgonyi, C. Au, T. Messina, R. K. Goodall, and H. R. Huff, "Oxygen precipitation behavior in 300 mm polished Czochralski silicon wafers," *J. Electrochem. Soc.* **146**(10), 3807–3811 (1999).
- ⁵B. Leroy and C. Plougonven, "Warping of silicon wafers," *J. Electrochem. Soc.* **127**(4), 961–970 (1980).
- ⁶H.-D. Chiou and L. W. Shive, "Test methods for oxygen precipitation in silicon," *VLSI Sci. Technol.* **1985**, 429.
- ⁷T. Y. Tan and C. Y. Kung, "Oxygen precipitation retardation and recovery phenomena in Czochralski silicon: Experimental observations, nuclei dissolution model, and relevancy with nucleation issues," *J. Appl. Phys.* **59**(3), 917–931 (1986).
- ⁸R. Swaroop, N. Kim, W. Lin, M. Bullis, L. Shive, A. Rice, E. Castel, and M. Christ, "Testing for oxygen precipitation in silicon wafers," *Solid State Technol.* **3**, 85–89 (1987).
- ⁹W. Huber and M. Pagani, "The behavior of oxygen precipitates in silicon at high process temperature," *J. Electrochem. Soc.* **137**(10), 3210–3213 (1990).
- ¹⁰G. A. Hawkins and J. P. Lavine, "The effect of rapid thermal annealing on the precipitation of oxygen in silicon," *J. Appl. Phys.* **65**(9), 3644–3654 (1989).
- ¹¹Q. Sun, K. H. Yao, H. C. Gatos, and J. Lagowski, "Effects of nitrogen on oxygen precipitation in silicon," *J. Appl. Phys.* **71**(8), 3760–3765 (1992).
- ¹²H. Abe, I. Suzuki, and H. Koya, "The effect of hydrogen annealing on oxygen precipitation behavior and gate oxide integrity in Czochralski Si wafers," *J. Electrochem. Soc.* **144**(1), 306–311 (1997).
- ¹³K. F. Kelton, R. Falster, D. Gambaro, M. Olmo, M. Cornara, and P. Wei, "Oxygen precipitation in silicon: Experimental studies and theoretical investigations within the classical theory of nucleation," *J. Appl. Phys.* **85**(12), 8097–8111 (1999).
- ¹⁴K. Nakai, Y. Inoue, H. Yokota, A. Ikari, J. Takahashi, A. Tachikawa, K. Kitahara, Y. Ohta, and W. Ohashi, "Oxygen precipitation in nitrogen-doped Czochralski-grown silicon crystals," *J. Appl. Phys.* **89**(8), 4301–4309 (2001).
- ¹⁵J. Haunschild, I. E. Reis, J. Geilker, and S. Rein, "Detecting efficiency-limiting defects in Czochralski-grown in silicon wafers in solar cell production using photoluminescence imaging," *Phys. Status Solidi Rapid Res. Lett.* **5**(5–6), 199–201 (2011).
- ¹⁶J. D. Murphy, K. Bothe, M. Olmo, V. V. Voronkov, and R. J. Falster, "The effect of oxide precipitates on minority carrier lifetime in p-type silicon," *J. Appl. Phys.* **110**, 053713 (2011).
- ¹⁷J. D. Murphy, K. Bothe, R. Krain, V. V. Voronkov, and R. J. Falster, "Parameterisation of injection-dependent lifetime measurements in semiconductors in terms of Shockley-Read-Hall statistics: An application to oxide precipitates in silicon," *J. Appl. Phys.* **111**, 113709 (2012).
- ¹⁸V. V. Voronkov and R. Falster, "Latent complexes of interstitial boron and oxygen dimers as a reason for degradation of silicon-based solar cells," *J. Appl. Phys.* **107**, 053509 (2010).
- ¹⁹S. Senkader, J. Esfandyari, and G. Hobler, "A model for oxygen precipitation in silicon including bulk stacking fault growth," *J. Appl. Phys.* **78**(11), 6469–6476 (1995).
- ²⁰S. Senkader, "Physical modeling and simulation of oxygen precipitation in silicon," Doctoral dissertation (Vienna University of Technology, 1996).
- ²¹B. G. Ko and K. D. Kwack, "Growth/dissolution model for oxygen precipitation based on the kinetics of phase transformations," *J. Appl. Phys.* **85**(4), 2100–2107 (1999).
- ²²K. Sueoka, M. Akatsuka, M. Okui, and H. Katahama, "Computer simulation for morphology, size, and density of oxide precipitates in CZ silicon," *J. Electrochem. Soc.* **150**(8), G469–G475 (2003).
- ²³A. Haarahluntunen, H. Väinölä, O. Anttila, M. Yli-Koski, and J. Sinkkonen, "Experimental and theoretical study of heterogeneous iron precipitation in silicon," *J. Appl. Phys.* **101**(4), 043507 (2007).
- ²⁴See supplementary material at <http://dx.doi.org/10.1063/1.4849435> for MATLAB source code.
- ²⁵H. Bender, "Investigation of the oxygen-related lattice defects in Czochralski silicon by means of electron microscopy techniques," *Phys. Status Solidi A* **86**, 245–261 (1984).
- ²⁶W. A. Tiller, S. Hahn, and F. A. Ponce, "Thermodynamic and kinetic considerations on the equilibrium shape for thermally induced microdefects in Czochralski silicon," *J. Appl. Phys.* **59**(9), 3255–3266 (1986).
- ²⁷J. Vanhellemont and C. Claeys, "A theoretical study of the critical radius of precipitates and its application to silicon oxide in silicon," *J. Appl. Phys.* **62**(9), 3960–3967 (1987).
- ²⁸W. Bergholz, M. J. Binns, G. R. Booker, J. C. Hutchison, S. H. Kinder, S. Messoloras, R. C. Newman, R. J. Stewart, and J. G. Wilkes, "A study of oxygen precipitation in silicon using high-resolution transmission electron microscopy, small-angle neutron scattering, and infrared absorption," *Philos. Mag. B* **59**(5), 499–522 (1989).
- ²⁹S. T. Dunham, "Modeling of the kinetics of dopant precipitation in silicon," *J. Electrochem. Soc.* **142**, 2823 (1995).
- ³⁰S. Kobayashi, "A model for oxygen precipitation in Czochralski silicon during crystal growth," *J. Cryst. Growth* **174**, 163–169 (1997).
- ³¹S. Kobayashi, "Mathematical modeling of grown-in defects formation in Czochralski silicon," *J. Cryst. Growth* **180**, 334–342 (1997).
- ³²W. J. Taylor, U. M. Gösele, and T. Y. Tan, "Precipitate strain relief via point defect interaction: Models for SiO₂ in silicon," *Mater. Chem. Phys.* **34**, 166–174 (1993).
- ³³P. Deák, L. C. Snyder, and J. W. Corbett, "Theoretical studies on the core structure of the 450 °C oxygen thermal donors in silicon," *Phys. Rev. B* **45**(20), 11612–11626 (1992).
- ³⁴W. Götz, G. Pensl, and W. Zulehner, "Observation of five additional thermal donor species TD12 to TD16 and of regrowth of thermal donors at initial stages of the new oxygen donor formation in Czochralski-grown silicon," *Phys. Rev. B* **46**(7), 4312–4315 (1992).
- ³⁵L. I. Murin, T. Hallberg, V. P. Markevich, and J. L. Lindström, "Experimental evidence of the oxygen dimer in silicon," *Phys. Rev. Lett.* **80**(1), 93–96 (1998).
- ³⁶S. Öberg, C. P. Ewels, R. Jones, T. Hallberg, J. L. Lindström, L. I. Murin, and P. R. Briddon, "First state of oxygen aggregation in silicon: The oxygen dimer," *Phys. Rev. Lett.* **81**(14), 2930–2933 (1998).
- ³⁷R. C. Newman, "Oxygen diffusion and precipitation in Czochralski silicon," *J. Phys.: Condensed Matter* **12**, R335–R365 (2000).
- ³⁸M.-H. Du, H. M. Branz, R. S. Crandall, and S. B. Zhang, "Bistability-mediated carrier recombination at light-induced boron-oxygen complexes in silicon," *Phys. Rev. Lett.* **97**(25), 256602 (2006).
- ³⁹G. Kresse and J. Furthmüller, "Efficient iterative schemes for ab initio total-energy calculations using a plane-wave basis set," *Phys. Rev. B* **54**(16), 11169–11186 (1996).
- ⁴⁰I. Clejan and S. T. Dunham, "A reduced moment-based model for precipitation kinetics and application to dopant activation in silicon," *J. Appl. Phys.* **78**(12), 7327–7333 (1995).
- ⁴¹H.-W. Guo, S. T. Dunham, C.-L. Shih, and C. Ahn, "Modeling of defect evolution and TED under stress based on DFT calculations," in *Proceedings of the International Conference on Simulation of Semiconductor Processes and Devices 2006*, pp. 71–74, 2006.
- ⁴²J. P. Hirth and J. Lothe, *Theory of Dislocations*, 2nd ed. (Wiley, New York, 1982).
- ⁴³S. T. Dunham, "Growth kinetics of disk-shaped extended defects with constant thickness," *Appl. Phys. Lett.* **63**, 464–466 (1993).
- ⁴⁴M. Schrems, T. Brabec, M. Budil, H. Pötzl, E. Guerrero, D. Huber, and P. Pongratz, "Simulation of oxygen precipitation in Czochralski grown silicon," *Mater. Sci. Eng., B* **4**, 393–399 (1989).
- ⁴⁵"ASTM standard test method for interstitial oxygen content of silicon by infrared absorption," in *Annual Book of ASTM Standards*, Vol. 43, 1983.
- ⁴⁶H.-D. Chiou, "Oxygen precipitation behavior and control in silicon crystals," *Solid State Technol.* **30**(3), 77–81 (1987).
- ⁴⁷H. W. Kennel, "Physical modeling of oxygen precipitation, defect formation, and diffusion in silicon," Doctoral dissertation (Stanford University, 1991).
- ⁴⁸W. L. Bond and W. Kaiser, "Interstitial versus substitutional oxygen in silicon," *J. Phys. Chem. Solids* **16**, 44–45 (1960).

- ⁴⁹A. Giannattasio, J. D. Murphy, S. Senkader, R. J. Falster, and P. R. Wilshaw, "Oxygen and nitrogen transport in silicon investigated by dislocation locking experiments," *J. Electrochem. Soc.* **152**(6), G460–G467 (2005).
- ⁵⁰R. J. Stewart, S. Messoloras, and S. Rycroft, "A small angle neutron scattering study of oxygen precipitation in silicon," in *Proceedings of the NATO Advanced Research Workshop, Exeter, UK*, 1996.
- ⁵¹K. Sueoka, N. Ikeda, and T. Yamamoto, "Morphology and size distribution of oxide precipitates in as-grown Czochralski silicon crystals," *Appl. Phys. Lett.* **65**(13), 1686–1688 (1994).
- ⁵²J. C. Mikkelsen, "The diffusivity and solubility of oxygen in silicon," *MRS Proc.* **59**, 19–30 (1986).
- ⁵³H. Bracht, N. A. Stolwijk, and H. Mehrer, "Properties of intrinsic point defects in silicon determined by zinc diffusion experiments under nonequilibrium conditions," *Phys. Rev. B* **52**(23), 16542 (1995).
- ⁵⁴H. Bracht, H. H. Silvestri, I. D. Sharp, and E. E. Haller, "Self- and foreign-atom diffusion in semiconductor isotope heterostructures. II. Experimental results for silicon," *Phys. Rev. B* **75**(3), 035211 (2007).
- ⁵⁵S. K. Ghandhi, *VLSI Fabrication Principles: Silicon and Gallium Arsenide* (John Wiley & Sons, New York, 1983).
- ⁵⁶R. Hull, *Properties of Crystalline Silicon* (Institute of Engineering and Technology, 1999), Vol. 20.
- ⁵⁷B. El-Kareh, *Fundamentals of Semiconductor Processing Technologies* (Kluwer, Boston, 1995).
- ⁵⁸A. Polian, V.-T. Dung, and P. Richet, "Elastic properties of a-SiO₂ up to 2300 K from Brillouin scattering measurements," *Europhys. Lett.* **57**(3), 375–381 (2002).
- ⁵⁹F. Liu, M. Mostoller, V. Milman, M. F. Chisholm, and T. Kaplan, "Electronic and elastic properties of edge dislocations in Si," *Phys. Rev. B* **51**, 17192 (1995).